








Compact laser modulation system for a transportable atomic gravimeter

A. LÓPEZ-VÁZQUEZ,¹ M. A. MALDONADO,¹ E. GOMEZ,^{1,*}  N. V. CORZO,² E. DE CARLOS-LÓPEZ,³ J. A. FRANCO VILLAFANE,⁴ K. JIMÉNEZ-GARCÍA,² J. JIMÉNEZ-MIER,⁵  J. L. LÓPEZ-GONZÁLEZ,¹ C. J. LÓPEZ-MONJARAZ,² J. M. LÓPEZ-ROMERO,² A. MEDINA HERRERA,² R. MÉNDEZ-FRAGOSO,⁶ C. A. ORTIZ,³  H. PEÑA,² J. G. RABOÑO BORBOLLA,² F. RAMÍREZ-MARTÍNEZ,⁵  AND V. M. VALENZUELA⁷ 

¹Instituto de Física, Universidad Autónoma de San Luis Potosí, 78290, San Luis Potosí, Mexico

²Centro de Investigación y de Estudios Avanzados del Instituto Politécnico Nacional-Unidad Querétaro, 76230, Querétaro, Mexico

³Centro Nacional de Metrología, CENAM, km 4.5 Carretera a los Cués, El Marqués, 76246, Querétaro, Mexico

⁴CONACYT-Instituto de Física, Universidad Autónoma de San Luis Potosí, 78290, San Luis Potosí, Mexico

⁵Instituto de Ciencias Nucleares, UNAM. Circuito Exterior, Ciudad Universitaria, 04510, Ciudad de México, Mexico

⁶Facultad de Ciencias, UNAM. Circuito Exterior, Ciudad Universitaria, 04510, Ciudad de México, Mexico

⁷Facultad de Ciencias Físico Matemáticas, Universidad Autónoma de Sinaloa, 80013, Sinaloa, Mexico

*egomez@ifisica.uaslp.mx

Abstract: Nowadays, atom-based quantum sensors are leaving the laboratory towards field applications requiring compact and robust laser systems. Here we describe the realization of a compact laser system for atomic gravimetry. Starting with a single diode laser operating at 780 nm and adding only one fiber electro-optical modulator, one acousto-optical modulator and one laser amplifier we produce laser beams at all the frequencies required for a Rb-87 atomic gravimeter. Furthermore, we demonstrate that an atomic fountain configuration can also be implemented with our laser system. The modulated system reported here represents a substantial advance in the simplification of the laser source for transportable atom-based quantum sensors that can be adapted to other sensors such as atomic clocks, accelerometers, gyroscopes or magnetometers with minor modifications.

© 2023 Optica Publishing Group under the terms of the [Optica Open Access Publishing Agreement](#)

1. Introduction

Atom interferometry has experienced fast and continuous growth since its introduction in 1991 [1,2]. Its first applications were oriented toward answering basic research and primary metrology questions. Some examples are related to precise measurements of the fine structure constant [3,4], or the Newtonian gravitational constant [5,6]. It has also been used to test general relativity [7,8], the isotropy of gravitational interaction [9,10], the equivalence principle [11–13], or in the search for new forces [14–16].

Practical applications of atom interferometry have multiplied over the last three decades. In inertial systems, it has been used to measure acceleration, including rotation [17–25], the local value of the acceleration of gravity g [26–31], or its gradient [32–35]. It has also been used in seismology or navigation systems [27,36]. Naturally, atom interferometers have evolved from complicated setups in research laboratories to practical, and in some cases transportable,

instruments. There are examples showing different degrees of progress for gravity measurements with atomic interferometers that occur in land [30,31,37], sea [38], air [19,39,40], and space [21].

The migration from the laboratory to the field imposes important restrictions on the design of atomic gravimeters. However, these restrictions also lead to the continuous improvement of the atom interferometer elements. Critical components of these systems are the light sources used to cool, trap and detect atoms, and the sources of Raman beams used to manipulate the atomic wave functions. These sources must be lightweight, compact, and robust for practical field instruments, capable of providing the necessary intensity without losing the phase coherence. Several examples of laser systems meet some of these needs [41–46]. For rubidium-based gravimeters, one option uses lasers at 1560 nm that are modulated, amplified, and eventually frequency-doubled to reach 780 nm [43,45–48]. This strategy takes advantage of the maturity of the telecom-band technology with many fiber-coupled components. An alternative is to start with lasers already at the desired wavelength of 780 nm in order to avoid the need for frequency doubling. To reach precise frequencies, the seed laser can be fixed and using modulators the frequency can be shifted and the laser beam controlled [37,41,49], or one can make use of agile tunable lasers with fine frequency control [50–52]. Micro-integrated systems produce very compact laser sources, including amplification and fiber-coupled beam output [42,53]. The ultimate goal is to use a single laser source modulated to produce all the frequencies needed [54,55]. Reaching this usually requires suppression of unwanted sidebands [45,46,55–58].

This contribution presents a design in which all the laser beams are obtained from a single laser source whose frequency is at the D_2 transition of the atomic rubidium (780 nm). The system does not require frequency doubling and uses a minimum of components improving its portability and stability. For example, the laser system in Ref. [47] requires four lasers, five optical frequency doublers, one electro-optical modulator, two-acousto optical modulators, four amplifiers, six optical benches to distribute the beams, and several feedback loops, in particular for phase locking the Raman beams. In comparison, our system requires one laser, one electro-optical modulator, one acousto-optical modulator, one amplifier and one optical bench. References [50,51] show other compact systems that use a single seed laser at 780 nm and allow for the implementation of sensitive gravimeters, with an alternative configuration to the one we present here. Their system shifts constantly the laser frequency at each stage of the sequence, whereas in our system the laser frequency is fixed, which contributes to the frequency stability. The time to change between frequencies is reduced considerably since it is no longer limited by the locking bandwidth. An interesting feature of our system is that we can direct all the light to multiple independent fibers, giving more flexibility for the applicability to other types of sensors. Even more, our system allows for the implementation of an atomic fountain and requires no optical phase lock loops since all the beam (including the Raman) are obtained from a common laser using modulation. A calcite crystal and a linear polarizer are used to suppress the unwanted sidebands [57,59]. All of this is achieved without losing the precision and the robustness required for metrology applications. Some of the above features are exclusive of the configuration we present. Our configuration represents a simplification compared to other reported setups [60–62] that translates into a compact (it fits on a 31×31 cm² aluminum plate), lightweight system that is built from commercially available components [63–66].

2. Laser system for atomic manipulation

Here we focus on the laser modulation system that generates all required beams and frequencies. The light from an external-cavity laser (New Focus SWL 7513) frequency-locked to an atomic reference goes through a fibered electro-optic modulator (FEOM, WPM-P78P78-ALO) (Fig. 1) that produces sidebands at the frequencies needed for the gravimetric sequence. The output of the FEOM is amplified (TA-7613) and then goes through an acousto-optic modulator (AOM) fed in both directions. This modulator serves to switch the beams on and off and direct them to the

desired output fiber. By selecting the radio frequency injected to the AOM, opposite beams are deflected in different pairs of directions labeled as *Trap a - Trap b*, *Path 2a-Path 2b*, and *Path 3b-Raman* in Fig. 1. The zero-order of the AOM determines the direction denoted as *Trap 0*.

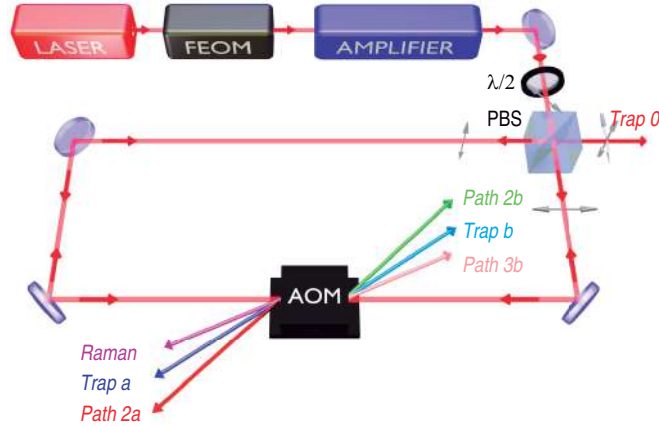


Fig. 1. Laser modulation system. FEOM: Fiber Electro-Optical Modulator, PBS: Polarization Beam Splitter, $\lambda/2$: half-wave retarder, AOM: Acousto-Optic Modulator. The FEOM generates the required frequencies and the AOM deflects the beam in pairs of directions.

The central frequency (350 MHz) of the AOM and its bandwidth (100 MHz) are large enough to have a good separation between the deflected beams, but small enough to maintain a good diffraction efficiency. Carefully placed pick-up mirrors send the beams through independent paths. When selecting a particular direction, the residual light that remains coupled in the wrong path is suppressed by 14 dB after the pick-up mirror and by 55 dB at the fiber output. Each path is equipped with mechanical shutters that prevent any residual light from reaching the atoms by keeping that path blocked while it is not in use.

The time sequence of a given experiment starts with the path *Trap 0* that collects the atoms in a magneto-optical trap (MOT) with a high loading rate (region R_1 in Fig. 2). Then one turns on the path *Trap a-Trap b* to keep the atoms in the MOT and to implement an optical molasses and a moving molasses to launch the atoms upwards. As the atoms cross the preparation region (R_2), the beams are directed to *Path 2a-Path 2b* to do the optical pumping, then one deflects the beam to *Raman*, to select a velocity from the whole velocity distribution and then back to *Path 2a-Path 2b* to apply a push beam to remove the atoms in the undesired state. The atoms then reach the free fall region (R_3), where one applies the Raman pulses for the interferometric sequence by deflecting the beam in the *Raman* path (*Path 3b* is not needed for the sequence and is free for other uses). The atoms finally fall into the detection region (R_2) where one measures the fraction of atoms in each hyperfine level by using the deflection to *Path 2a-Path 2b*. We explain below in detail how to implement each of these steps with the simple laser modulation system of Fig. 1.

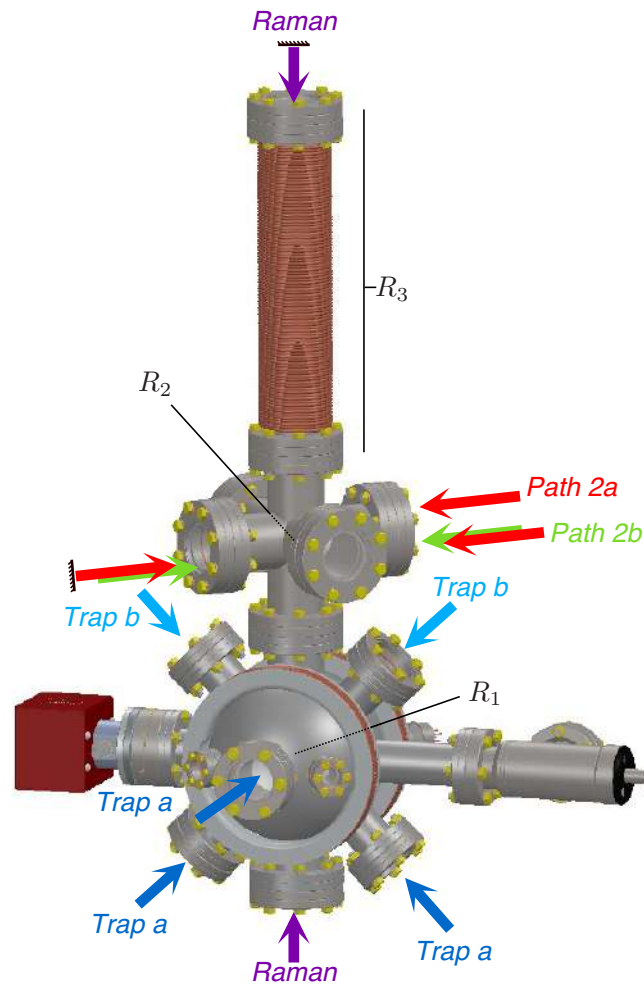


Fig. 2. Schematic of the beams and regions of the vacuum chamber in the quantum gravimeter. R_1 : trapping region, R_2 : state preparation and measurement region, R_3 : interferometric sequence region. The horizontal MOT beam is retro-reflected. *Trap 0* shares the paths of *Trap a* and *b*. The color code of the beams follow that of Fig. 1.

3. Trapping and optical molasses

The diode laser is locked to the $5S_{1/2} F=2 \rightarrow 5P_{3/2} F=3$ transition in ^{85}Rb . This gives a stable frequency reference with a large enough detuning from the transitions in ^{87}Rb , which will be important when applying the Raman transitions. First, we describe how to get a MOT using the *Trap 0* direction. Figure 3(a) shows the trapping frequency ν_T , which is red-detuned by 14 MHz from the cycling transition $5S_{1/2} F=2 \rightarrow 5P_{3/2} F=3$, and the repumping frequency ν_R that is set in resonance with the transition $5S_{1/2} F=1 \rightarrow 5P_{3/2} F=1$, both in ^{87}Rb . The laser is locked at the frequency ν_L (Fig. 3(b)), and the FEOM is modulated simultaneously at two frequencies to create the sidebands required for the trap and repumper at frequencies ν_1 and ν_3 respectively. The microwave frequencies that are fed to the FEOM for this and other steps in the sequence are listed in [Supplement 1](#). The extra sidebands that are present are strongly detuned and have a negligible effect on the MOT performance. In addition, the repumper sideband (ν_3) power is maintained 12 times smaller than the trap (ν_T) to minimize the non-linearities, as discussed in detail further below.

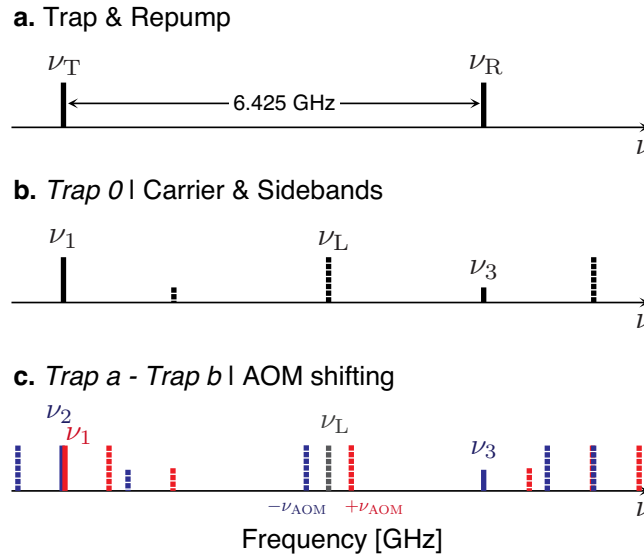


Fig. 3. a) Frequencies required for the MOT and molasses, with the trap (ν_T) and the repumper (ν_R) beams. b) Carrier (ν_L) and sidebands (ν_1 and ν_3) when using the *Trap 0* path. c) Using the *Trap a-Trap b* pair the carrier is shifted in frequency ($+\nu_{\text{AOM}}$ in red and $-\nu_{\text{AOM}}$ in blue) giving the trapping beams (ν_1 and ν_2) and the repumper (ν_3). All the other unused first-order sidebands are also shown as dotted lines.

A tapered amplifier increases and stabilizes the power at 500 mW. The *Trap 0* path is not diffracted by the AOM and goes out in the other port of the polarization beam splitter (PBS) in Fig. 1. The light is coupled via optical fibers and sent out to a preliminary vacuum system to test the trapping and cooling stages for the quantum gravimeter. The *Trap 0* beams are sent through the same optical fibers as the *Trap a* and *Trap b* beams (Fig. 2). Each beam at the MOT is collimated to a $(1/\sqrt{e})$ radius of 2.7 mm, and we use a magnetic field gradient of 0.6 mT cm^{-1} .

The *Trap 0* path provides a good loading rate (due to its higher optical power), but it does not offer the required flexibility on frequency tuning of the beams for the subsequent steps, particularly for the implementation of a moving molasses. After some loading time, we switch to having a MOT with the *Trap a-Trap b* pair (Fig. 3(c)). We take the +1 (-1) order of the beams traveling to the right (left) on the AOM so that they are shifted by similar opposite amounts in frequency ($\pm\nu_{\text{AOM}}$). To create the sidebands required for trapping ν_1 and ν_2 correspond to the

trapping beams and ν_3 to the repumping beam), the FEOM is modulated simultaneously at three frequencies. The beams with frequency ν_1 go through the path indicated by *Trap a* while the beams ν_2 go through *Trap b* in Fig. 2. Each of the carrier beams displaced in frequency from ν_L by the AOM (red and blue in Fig. 3) have sidebands at the three modulating frequencies (shown here only up to first order). The frequencies of these and other higher-order non-linearities must be analyzed and their effect minimized.

It is easy to move to an optical molasses or a moving molasses from this point since we have independent control of the frequency of the beams ν_1 and ν_2 just by changing the frequency of the microwaves injected into the FEOM. Shifting ν_1 and ν_2 simultaneously by the same amount and turning off the magnetic gradient, we obtain an optical molasses, and by keeping one fixed and changing the other, we obtain a moving molasses that is used to launch atoms against gravity in an atomic fountain configuration.

In our experiment, the intensity of the trapping beams on the *Trap a-Trap b* configuration is 3.8 mW cm^{-2} , which gives us a loading rate of $3.2 \pm 0.5 \times 10^6$ atoms per second at a vapor pressure below 10^{-10} Torr. The loading rate using the *Trap 0* path is 4.2 times higher than that of the *Trap a-Trap b* configuration. These results should improve in the future once move to a 2 W tapered amplifier. We note that the FEOM is made out of Potassium Titanyl Phosphate (KTP) and it can handle a relatively high laser power. After the MOT, when the optical molasses is applied, the temperature of the atomic cloud is reduced by a factor of 5. By keeping ν_1 fixed and changing ν_2 , we confirmed that we could control the atoms' vertical launch velocity to a particular desired value, which was measured by imaging the atomic cloud with a short resonant retro-reflected vertical probe pulse at different delays. In summary, this section demonstrates a properly working MOT, optical molasses and moving molasses with the laser system.

4. State preparation, interferometric sequence and measurement

This section shows how the laser system of Fig. 1 generates the rest of the pulses required for implementing the atomic gravimeter, such as the state preparation, the Raman pulses and the measurement sequence. The critical steps of the MOT, molasses and moving molasses were demonstrated in a preliminary vacuum chamber; the other steps require the complete vacuum chamber (Fig. 2). Since the emphasis here is to present the laser system, we verified that the required frequencies were indeed generated and deflected towards the correct optical fiber.

After the cold atoms are launched upwards with the moving molasses, they would reach region R_2 (Fig. 2) and cross through the beams responsible for state preparation. The beams originate from the pair *Path 2a-Path 2b*. Once more, each of these paths is shifted on opposite orders of the AOM. The optical pumping to the $5S_{1/2} F=2 m_F=0$ level is achieved by having one beam tuned to the $5S_{1/2} F=1 \rightarrow 5P_{3/2} F=1$ transition (ν_R and ν_5) and a second beam on the $5S_{1/2} F=2 \rightarrow 5P_{3/2} F=2$ transition (ν_P and ν_4) in ^{87}Rb (Figs. 4(a) and 4(b)), as has been shown before [57]. The latter must have π polarization, and both of them are retro-reflected. We overlap the two beams in a polarizing beam splitter to have orthogonal polarization before sending them through a polarization-maintaining fiber.

A particular velocity is selected through a Raman transition using the counter-propagating vertical beams coupling the hyperfine levels $5S_{1/2} F=2 m_F=0 \rightarrow 5S_{1/2} F=1 m_F=0$. This transition is generated with light from the *Raman* path (Fig. 1) that is modulated on the FEOM at a frequency close to the hyperfine splitting (ν_6 and ν_7 in Fig. 4(c) correspond to the Raman pair), in the same way as Ref. [57]. The atoms that remain in the wrong state are removed with a push beam tuned to the $5S_{1/2} F=2 \rightarrow 5P_{3/2} F=3$ cycling transition (ν_8 in Fig. 4(d)). This push beam is taken from *Path 2b*, goes through the same fiber as the optical pumping, and a part of it is displaced slightly upward in region R_2 without being retro-reflected. The optical pumping and push beams do not interfere since they interact with the atoms at different positions and times during the sequence.

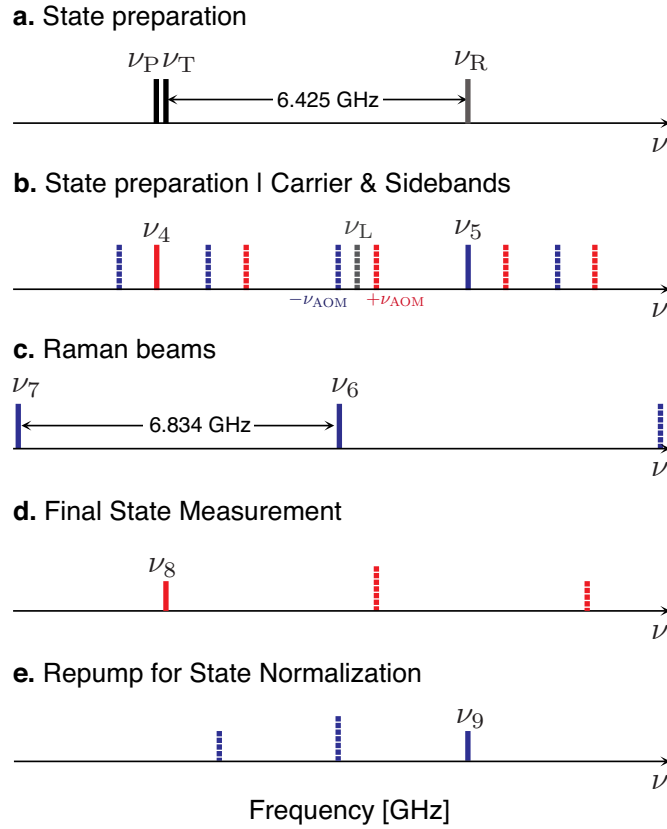


Fig. 4. Carrier and sidebands required for: b) the state preparation, c) Raman beams for the interferometric sequence, d) measurement of the final state, and e) repumping for state normalization. a) The transitions in ^{87}Rb . The colors and type of line follow the same code as in Fig. 3

The cloud of cold atoms reaches the magnetically shielded region R_3 (Fig. 2), where the interferometric measurement would be performed via the interaction with the $(\pi/2 - \pi - \pi/2)$ Raman pulses. The beam for this purpose is again extracted from the *Raman* path (Fig. 1) and modulated at a frequency near the hyperfine splitting of the $5S_{1/2}$ ground state (Fig. 4(c)). On their way down, the atoms reach region R_2 again, where the final state is read using three consecutive pulses from the pair *Path 2a-Path 2b* at the position where the beams are retro-reflected. First, the falling cloud of atoms is exposed to a pulse resonant with the cycling transition (ν_8 in Fig. 4(d)), then to a repumping pulse (ν_9 in Fig. 4(e)), and finally to another pulse tuned again to the cycling transition. This allows for detecting the number of atoms remaining in either of the two hyperfine sub-levels of the ground state and therefore, normalizes the interferometric measurement to the total number of atoms in the cloud [57].

5. Frequency mixing and non-linearities

The frequency at which the diode laser is locked is conveniently chosen to be one of the many resonances of the D_2 line in ^{85}Rb . To select the specific resonance to use, it is important to pay particular attention to both the compatibility of the microwave components, and to avoid problems with the extra sidebands and other non-linearities that appear at the sum and difference of the microwave frequencies applied for the modulation (see Supplement 1 for supporting

content). The non-linearities are dominated by the FEOM [49], and their heights can be limited by reducing the modulating power. Taking a single modulation frequency (ν_a), the n -th sideband has an electric field reduced by a factor $J_n(\beta_a)$, the Bessel function of order n with modulation index β_a . Adding a second modulation frequency (ν_b) introduces sidebands that mix the two frequencies. For example, the first-order sideband of ν_a modulated at β_a combines with that of ν_b modulated at β_b to produce sidebands at frequencies $\nu_a + \nu_b$ and $\nu_a - \nu_b$ with an electric field reduced by a factor $J_1(\beta_a)J_1(\beta_b)$ (see [Supplement 1](#) for supporting content). The height and frequency of the non-linearities have been measured by sending the modulated light through a Fabry Perot cavity at different microwave powers. In this way, by determining the half-wave voltage (V_π) to calibrate each frequency's modulation index (β), it was indeed verified that the non-linearities follow the above mentioned dependence on Bessel functions.

In all the steps in the sequence that contain a single modulation frequency (ν) in Figs. 3 and 4, it was only necessary to ensure that higher-order sidebands separated by $n\nu$ lie sufficiently far away from any resonance, typically by a few GHz. As the number of modulation frequencies sent to the FEOM increases, a higher number of non-linearities at the sum and difference of the modulating frequencies are present, and there is a higher probability of getting close to a particular resonance. The scattering rate of these non-linearities must be negligible compared with that of the beam that is desired to interact with the atomic population during any particular step in the sequence. Special attention needs to be paid to steps involving three simultaneous frequencies, as is the case for the MOT and molasses, particularly because they require off-resonant beams.

The blue squares in Fig. 5 show the power of the frequencies present at the output of the modulator up to third-order, normalized to that of the carrier. The figure corresponds to the MOT configuration with three frequencies injected into the FEOM (Fig. 3(c)) for our experimental settings. The two "carriers" are shifted by $\pm\nu_{\text{AOM}}$, respectively. The modulation required to generate ν_1 and ν_2 creates additional frequencies with approximately the same power, as can be seen from the group of squares along the same horizontal line as the blue circle in Fig. 5. Higher-order non-linearities form additional frequencies arranged in horizontal groups of decreasing power. The repumper (empty blue triangle) has a smaller power than the trapping beams (empty blue circle) due to the reduced modulation at that frequency. The red diamonds in Fig. 5 show the calculation of the scattering rate of all the frequencies appearing up to third-order normalized to that of the repumper. The trapping beams are detuned from resonance and have a slightly smaller scattering rate (filled red circle) than the repumper (filled red triangle). Even when there are many additional frequencies present, their scattering rate is much smaller than that of the trap and repumper beams.

Most of the spurious frequencies have a scattering rate (filled red diamonds) similar or smaller than that of the carrier, indicated by c in Fig. 5. In other words, the presence of most of the sidebands for all the steps in the sequence is as potentially harmless as that due to the presence of the carrier that is more than two GHz away from resonance, and most of them are below the lowest value in the plot. As we move to higher-order terms, the scattering is reduced either by their detuning or their power. Keeping the repumper power a factor of 12 times lower than that of the trapping beams, helps suppress the non-linearities owing to the dependence on the Bessel function (see [Supplement 1](#) for supporting content). We use a modulating power for the trapping beams of 16.5 dBm, giving first-order sidebands with 15 % power compared to the carrier, to help reducing the power of the non-linearities.

The spurious frequency closest to a particular resonance during the molasses is still 261 MHz away, except for a third-order non-linearity that includes the three modulation frequencies and appears at the repumper transition (c in Fig. 5). Fortunately, since it has lower power and is at the repumper frequency, it has little effect on the performance of the trap. Still, this spurious frequency, as well as that indicated by b (scattering from the blue line to the left of ν_2 in Fig. 3(c)) in Fig. 5, may be responsible for making the trap positions a little less stable than the one we

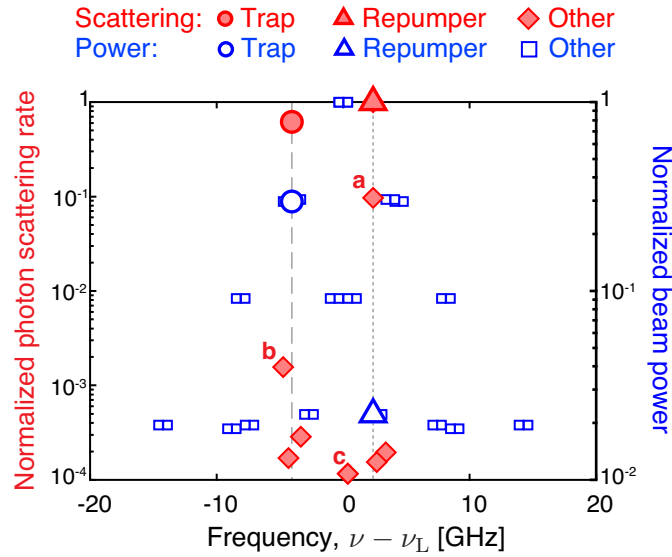


Fig. 5. Scattering rate (filled diamonds) and power (empty squares) of the frequencies appearing after modulation as a function of frequency relative to the diode laser (ν_L). The scattering rate is normalized to that of the repumper (filled triangle), while the power is normalized to that of the carrier (empty squares at the top). The vertical lines correspond to the repumper (short dashed) and cycling (long dashed) transition resonance. The points marked with a, b and c are discussed in the text.

obtained with the *Trap 0* path, as seen on the camera we use to image the atoms. The *Trap 0* configuration does not have this problem since it includes two and not three modulation frequencies. The scattering from these spurious frequencies has little effect on the trapping and cooling dynamics, as is confirmed experimentally by the fact that we have demonstrated the operation of standard and fully functional trap, molasses and moving molasses. The scattering of the additional frequencies may shift the trap position by less than $40 \mu\text{m}$, which would correspond to a change in the measurement smaller than $0.1 \mu\text{Gal}$ [67]. The effect of the non-linearities can be further suppressed by reducing the modulation at the expense of having less power for trapping. A similar analysis was made for the other steps in the sequence. The effect of the non-linearities in those steps is even smaller since they require less modulating frequencies (two or one instead of the three beams in the MOT and molasses), and also since they compete against resonant beams (in contrast to the off-resonant trapping beams).

6. System integration and control

Figure 6 shows the optics board containing all the modulation system elements with fiber outputs. Everything fits on a compact aluminum plate with dimensions $31 \text{ cm} \times 31 \text{ cm} \times 1.3 \text{ cm}$, thick enough to make it stable. This rather simple, robust and elegant arrangement produces all the beams required for a manipulation as complex as that required for the operation of an atomic gravimeter. Moreover, with minor modifications, it would also work for other cold atom sensors and almost any cold atom manipulation system. In addition, the footprint is smaller than that of other designs and with a minimum of optical components, something very desirable for transportable systems.

Each of the paths in Fig. 1 includes a mechanical shutter, most of them based on a step motor [63]. These shutters are mounted on a separate plate located below the optics board and joined to it by a layer of sorbothane to minimize vibrations, the effect of which is suppressed regardless,

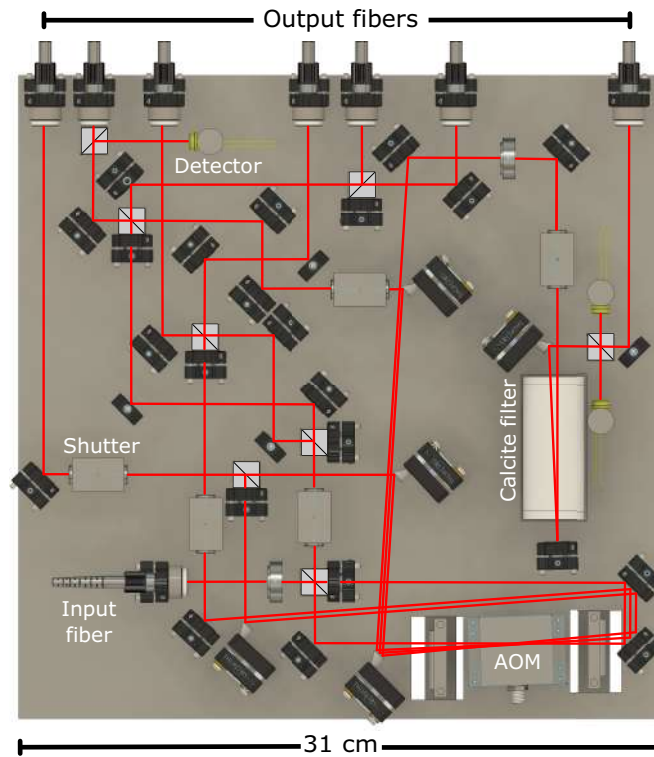


Fig. 6. Compact optical design for the modulation system. The input fiber corresponds to the output of the amplifier in Fig. 1. The beams are directed to some of the 7 output optical fibers depending on the step in the sequence.

given that the Raman beams follow the same path up to the retro-reflection mirror [59]. The Raman beam has a shutter based on an amplified piezo actuator (PK2FSF1). The large piezo displacement ($220\ \mu\text{m}$) and a tight beam focus ensure complete beam extinction [63]. The shutter has a speedy response, it can be opened in less than 1 ms, remain open for a time as small as 1 ms, which is essential for the Raman pulses, and it has a timing jitter below the $20\ \mu\text{s}$ limit of our measurement. The dimensions of the 19 in rack unit for optics are $42\ \text{cm} \times 46\ \text{cm} \times 13.4\ \text{cm}$ and has a weight of 9 kg.

Implementing the gravimetric sequence requires the application of up to three microwave frequencies simultaneously to the FEOM and a tunable RF frequency to the AOM. The frequencies are obtained from a combination of Direct Digital Synthesis (DDS) and Phase Lock Loops (PLL) (Fig. 7). For synthesizers 0, 1 and 2 a programmable DDS with four outputs (AD9959) generates a 100 MHz signal used as a clock for a PLL synthesizer (ADF4350), which is the one that generates the microwave signal. A list of values is programmed on the AD9959, and a trigger pulse from the control system moves to the next value on the list as the sequence proceeds. The change in frequency of the AD9959 produces a proportional change in frequency for the ADF4350. The microwave scan range using this method is limited to about 60 MHz, enough for the trapping and optical molasses. Synthesizer 0 is added to reach the value for the *Trap 0* configuration, which is outside this scanning range.

The phase noise on the microwaves is critical for the interferometric sequence; this requirement is considerably relaxed in all other steps, and simpler synthesizers (such as the ADF4350) can be used. A programmable low phase noise synthesizer (3 in Fig. 7, APSYN420) is used for the

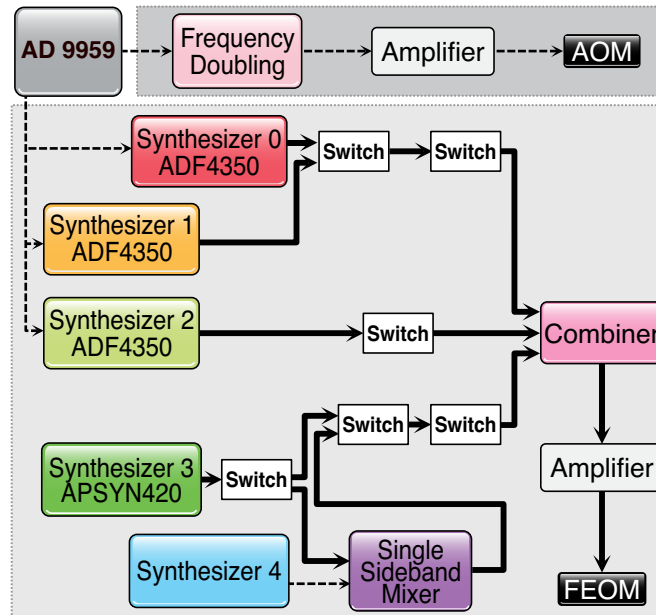


Fig. 7. Microwave system that produces the signals for the electro-optical modulator (FEOM) and acousto-optical modulator (AOM). Dashed and solid arrows correspond to RF and microwave signals respectively.

Raman beams with a fixed frequency close to the required one. The output is frequency shifted by Synthesizer 4 using a single sideband mixer (SSB4080A) [57,64,65]. This last synthesizer produces the frequency ramp centered at 150 MHz required for the gravimetric sequence [60].

A set of microwave switches enable the signals at the correct time in the sequence and reach a three-way microwave combiner (RFLT3W2G08G) that works from 2 to 8 GHz, covering the required frequency range. The digital pulses from the control system go through the listed values in Synthesizers 0 to 4 and enable the correct switches to obtain at the output of the combiner up to three frequencies simultaneously, that are amplified before going to the FEOM. The non-linearities introduced by the microwave combiner or amplifier are negligible, and most of them appear at the FEOM output [49].

The AOM frequency (ν_{AOM}) is produced by frequency doubling the output of the AD9959 to reach up to 400 MHz. The three deflection directions we use (Fig. 1) correspond to frequencies of 300, 350 and 400 MHz, but adding more deflection directions is possible for other sensors. In addition, frequency filters are added here and in the other components to remove unwanted spurious frequencies. The system is very stable in frequency since all the components are derived from DDS locked to an atomic clock (PRS10), a more precise option than using a VCO [49]. Most of the system is controlled with digital pulses produced from a compact Field-Programmable Gate Array (FPGA). All the electronics required to control the modulation system fit into a 19 in rack unit of dimensions 42 cm × 46 cm × 8.9 cm, and weight 9 kg (Fig. 8). The first version of the gravimeter will contain three parts: 1) all the units combined in a rack with dimensions 68 cm × 52 cm × 65.2 cm and a weight of 50 kg, 2) an electrical power rack of 37 cm × 47.6 cm × 48 cm and a weight of 56 kg, with a power consumption of about 270 W, 3) a vacuum chamber with dimensions 64 cm × 64 cm × 125 cm and a weight of 50 kg.

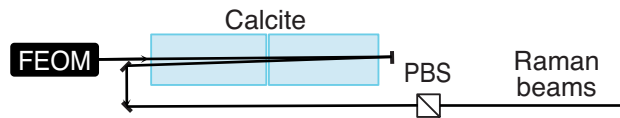
Generating the Raman beams from a single beam using a modulator has the advantages of simplicity, robustness and phase noise reduction. The drawback is the presence of extra sidebands that introduce a spatial modulation of the Rabi frequency [56,57], and other systematic



Fig. 8. Rack unit with all the electronics required to control the modulation system.

contributions [61]. We filter some of the undesired sidebands by adding a calcite crystal followed

a. Schematic of sideband filter



b. Relative strengths of Carrier and Sidebands

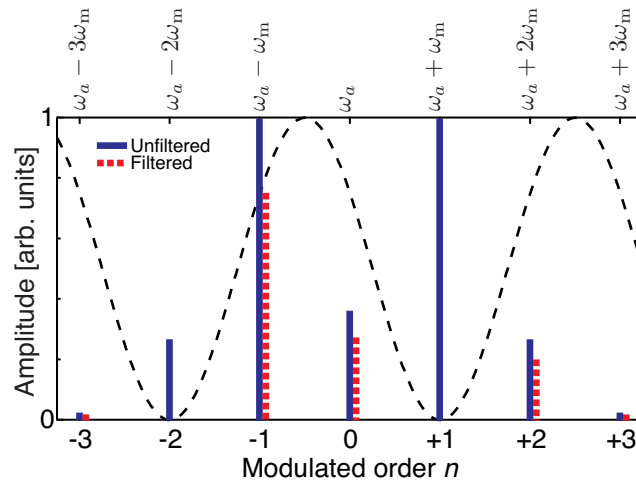


Fig. 9. Optical filtering by the calcite crystal and polarizer. The original modulated lines are shown in blue with a modulation index of $\beta = 1.78$, and in red the beams after the filtering. The dashed curve is the transmission through the filter. ω_a and ω_m are the carrier and modulation frequency respectively.

by a polarizer (Fig. 9) [57,59]. This combination gives a sinusoidal modulation of the output power as a function of laser frequency (dashed black line in Fig. 9). The crystal length of 7.9432 cm gives a free spectral range of 3×6.8 GHz. By changing the crystal temperature, we tuned the oscillations minima to the position of the +1 and -2 sideband that we were able to suppress by more than 20 dB. The dominant Raman pair is formed by the carrier and the -1 sideband, where each of them is reduced by 3 dB by the calcite crystal filter. A power ratio of 2.78 between the carrier and the -1 sideband cancels the light shift at 2.67 GHz detuning that we use for the Raman transition [62]. Without the calcite filter, another Raman pair would be formed by the carrier and the +1 sideband with the same power on the beams but a detuning of 4.16 GHz. The interference of the two Raman pairs produces a spatial modulation of the Rabi frequency [57] with variations as large as 78 %. The calcite filter eliminates this and many other higher-order Raman pairs, and the next pair that appears is the one composed of the +2 and +3 sidebands with a Rabi frequency smaller by a factor of 47, giving a spatial Rabi frequency modulation of 4.1 %.

7. Conclusions

We present a modulation system that generates all the beams and frequencies required to implement an atomic gravimeter. It uses only one laser, one electro-optical modulator, one acousto-optical modulator and one amplifier. Compared with other systems that start with a laser at 1560 nm, our system does all the modulation directly at 780 nm, eliminating the need for frequency doubling. The resulting system is very compact and well suited for transportable sensors due to the reduction in the footprint, complexity and power consumption. An exciting feature of the system is that it can both trap the atoms and also launch them in an atomic fountain configuration. Besides of allowing for longer free-fall times, the atomic fountain gives the atoms a large initial velocity, making it possible to immediately resolve spectrally the desired Raman transitions [66]. At the trapping and cooling stage, we simultaneously send up to three different frequencies to the electro-optical modulator and additional frequencies appear due to the non-linearities. We show that the trapping, cooling and launching of atoms works well even in the presence of detuned non-linearities. Other steps in the sequence require a smaller number of modulating frequencies and are less susceptible to non-linearities. For example, the Raman beams, which are critical for implementing the sensor, require only a single modulating signal and are free from this frequency mixing. Higher-order sidebands are still present with the modulation that introduce a spatial variation of the Rabi frequency. However, it has been shown that these sidebands can be eliminated and their effect suppressed by adding a filter based on a calcite birefringent crystal and a polarizer. This publication focuses on presenting and characterizing the complete laser system for the gravimetric manipulation. The operation and characterization of the complete sensor will be presented in a future publication.

Funding. Consejo Potosino de Ciencia y Tecnología (23871); Universidad Autónoma de San Luis Potosí; Consejo Nacional de Ciencia y Tecnología (260704, 316171, FC 157, Fordecyt 297126).

Disclosures. The authors declare no conflicts of interest.

Data availability. Data underlying the results presented in this paper are not publicly available at this time but may be obtained from the authors upon reasonable request.

Supplemental document. See [Supplement 1](#) for supporting content.

References

1. F. Riehle, T. Kisters, A. Witte, J. Helmcke, and C. J. Bordé, "Optical Ramsey spectroscopy in a rotating frame: Sagnac effect in a matter-wave interferometer," *Phys. Rev. Lett.* **67**(2), 177–180 (1991).
2. M. Kasevich and S. Chu, "Atomic interferometry using stimulated Raman transitions," *Phys. Rev. Lett.* **67**(2), 181–184 (1991).
3. R. Bouchendira, P. Cladé, S. Guellati-Khélifa, F. Nez, and F. Biraben, "New Determination of the Fine Structure Constant and Test of the Quantum Electrodynamics," *Phys. Rev. Lett.* **106**(8), 080801 (2011).

4. R. H. Parker, C. Yu, W. Zhong, B. Estey, and H. Müller, "Measurement of the fine-structure constant as a test of the Standard Model," *Science* **360**(6385), 191–195 (2018).
5. J. B. Fixler, G. T. Foster, J. M. McGuirk, and M. A. Kasevich, "Atom Interferometer Measurement of the Newtonian Constant of Gravity," *Science* **315**(5808), 74–77 (2007).
6. G. Rosi, F. Sorrentino, L. Cacciapuoti, M. Prevedelli, and G. M. Tino, "Precision measurement of the Newtonian gravitational constant using cold atoms," *Nature* **510**(7506), 518–521 (2014).
7. S. Dimopoulos, P. W. Graham, J. M. Hogan, and M. A. Kasevich, "Testing General Relativity with Atom Interferometry," *Phys. Rev. Lett.* **98**(11), 111102 (2007).
8. P. Asenbaum, C. Overstreet, T. Kovachy, D. D. Brown, J. M. Hogan, and M. A. Kasevich, "Phase Shift in an Atom Interferometer due to Spacetime Curvature across its Wave Function," *Phys. Rev. Lett.* **118**(18), 183602 (2017).
9. H. Müller, S.-w. Chiow, S. Herrmann, S. Chu, and K.-Y. Chung, "Atom-Interferometry Tests of the Isotropy of Post-Newtonian Gravity," *Phys. Rev. Lett.* **100**(3), 031101 (2008).
10. X.-C. Duan, X.-B. Deng, M.-K. Zhou, K. Zhang, W.-J. Xu, F. Xiong, Y.-Y. Xu, C.-G. Shao, J. Luo, and Z.-K. Hu, "Test of the Universality of Free Fall with Atoms in Different Spin Orientations," *Phys. Rev. Lett.* **117**(2), 023001 (2016).
11. M. G. Tarallo, T. Mazzoni, N. Poli, D. V. Sutyurin, X. Zhang, and G. M. Tino, "Test of Einstein Equivalence Principle for 0-Spin and Half-Integer-Spin Atoms: Search for Spin-Gravity Coupling Effects," *Phys. Rev. Lett.* **113**(2), 023005 (2014).
12. B. Barrett, L. Antoni-Micollier, L. Chichet, B. Battelier, P.-A. Gominet, A. Bertoldi, P. Bouyer, and A. Landragin, "Correlative methods for dual-species quantum tests of the weak equivalence principle," *New J. Phys.* **17**(8), 085010 (2015).
13. R. Geiger and M. Trupke, "Proposal for a Quantum Test of the Weak Equivalence Principle with Entangled Atomic Species," *Phys. Rev. Lett.* **120**(4), 043602 (2018).
14. M. Jaffe, P. Haslinger, V. Xu, P. Hamilton, A. Upadhye, B. Elder, J. Khoury, and H. Müller, "Testing sub-gravitational forces on atoms from a miniature in-vacuum source mass," *Nat. Phys.* **13**(10), 938–942 (2017).
15. P. Haslinger, M. Jaffe, V. Xu, O. Schwartz, M. Sonnleitner, M. Ritsch-Marte, H. Ritsch, and H. Müller, "Attractive force on atoms due to blackbody radiation," *Nat. Phys.* **14**(3), 257–260 (2018).
16. D. O. Sabulsky, I. Dutta, E. A. Hinds, B. Elder, C. Burrage, and E. J. Copeland, "Experiment to Detect Dark Energy Forces Using Atom Interferometry," *Phys. Rev. Lett.* **123**(6), 061102 (2019).
17. B. Canuel, F. Leduc, D. Holleville, A. Gauguier, J. Fils, A. Virdis, A. Clairon, N. Dimarcq, C. J. Bordé, A. Landragin, and P. Bouyer, "Six-Axis Inertial Sensor Using Cold-Atom Interferometry," *Phys. Rev. Lett.* **97**(1), 010402 (2006).
18. T. Müller, M. Gilowski, M. Zaiser, P. Berg, C. Schubert, T. Wendrich, W. Ertmer, and E. M. Rasel, "A compact dual atom interferometer gyroscope based on laser-cooled rubidium," *Eur. Phys. J. D* **53**(3), 273–281 (2009).
19. R. Geiger, V. Ménoret, G. Stern, N. Zahzam, P. Cheinet, B. Battelier, A. Villing, F. Moron, M. Lours, Y. Bidel, A. Bresson, A. Landragin, and P. Bouyer, "Detecting inertial effects with airborne matter-wave interferometry," *Nat. Commun.* **2**(1), 474 (2011).
20. A. Bonnin, N. Zahzam, Y. Bidel, and A. Bresson, "Simultaneous dual-species matter-wave accelerometer," *Phys. Rev. A* **88**(4), 043615 (2013).
21. B. Barrett, L. Antoni-Micollier, L. Chichet, B. Battelier, T. Lévêque, A. Landragin, and P. Bouyer, "Dual matter-wave inertial sensors in weightlessness," *Nat. Commun.* **7**(1), 13786 (2016).
22. I. Dutta, D. Savoie, B. Fang, B. Venon, C. L. Garrido Alzar, R. Geiger, and A. Landragin, "Continuous Cold-Atom Inertial Sensor with 1 nrad/sec Rotation Stability," *Phys. Rev. Lett.* **116**(18), 183003 (2016).
23. B. Fang, I. Dutta, P. Gillot, D. Savoie, J. Lautier, B. Cheng, C. L. G. Alzar, R. Geiger, S. Merlet, F. P. D. Santos, and A. Landragin, "Metrology with Atom Interferometry: Inertial Sensors from Laboratory to Field Applications," *J. Phys.: Conf. Ser.* **723**, 012049 (2016).
24. D. Savoie, M. Altorio, B. Fang, L. A. Sidorenkov, R. Geiger, and A. Landragin, "Interleaved atom interferometry for high-sensitivity inertial measurements," *Sci. Adv.* **4**(12), eaau7948 (2018).
25. B. Barrett, P. Cheiney, B. Battelier, F. Napolitano, and P. Bouyer, "Multidimensional Atom Optics and Interferometry," *Phys. Rev. Lett.* **122**(4), 043604 (2019).
26. A. Peters, K. Y. Chung, and S. Chu, "Measurement of gravitational acceleration by dropping atoms," *Nature* **400**(6747), 849–852 (1999).
27. M. de Angelis, A. Bertoldi, L. Cacciapuoti, A. Giorgini, G. Lamporesi, M. Prevedelli, G. Saccorotti, F. Sorrentino, and G. M. Tino, "Precision gravimetry with atomic sensors," *Meas. Sci. Technol.* **20**(2), 022001 (2009).
28. D. Schlippert, J. Hartwig, H. Albers, L. L. Richardson, C. Schubert, A. Roura, W. P. Schleich, W. Ertmer, and E. M. Rasel, "Quantum Test of the Universality of Free Fall," *Phys. Rev. Lett.* **112**(20), 203002 (2014).
29. C. Freier, M. Hauth, V. Schkolnik, B. Leykauf, M. Schilling, H. Wziontek, H.-G. Scherneck, J. Müller, and A. Peters, "Mobile quantum gravity sensor with unprecedented stability," *J. Phys.: Conf. Ser.* **723**, 012050 (2016).
30. V. Ménoret, P. Vermeulen, N. Le Moigne, S. Bonvalot, P. Bouyer, A. Landragin, and B. Desruelle, "Gravity measurements below 10^{-9} g with a transportable absolute quantum gravimeter," *Sci. Rep.* **8**(1), 12300 (2018).
31. X. Wu, Z. Pagel, B. S. Malek, T. H. Nguyen, F. Zi, D. S. Scheirer, and H. Müller, "Gravity surveys using a mobile atom interferometer," *Sci. Adv.* **5**(9), eaax0800 (2019).
32. J. M. McGuirk, G. T. Foster, J. B. Fixler, M. J. Snadden, and M. A. Kasevich, "Sensitive absolute-gravity gradiometry using atom interferometry," *Phys. Rev. A* **65**(3), 033608 (2002).

33. N. Metje, D. N. Chapman, C. D. F. Rogers, and K. Bongs, "Seeing through the Ground: The Potential of Gravity Gradient as a Complementary Technology," *Adv. Civil Eng.* **2011**, 1–9 (2011).
34. F. Sorrentino, Q. Bodart, L. Cacciapuotì, Y.-H. Lien, M. Prevedelli, G. Rosi, L. Salvi, and G. M. Tino, "Sensitivity limits of a Raman atom interferometer as a gravity gradiometer," *Phys. Rev. A* **89**(2), 023607 (2014).
35. B. Stray, A. Lamb, A. Kaushik, J. Vovrosh, A. Rodgers, J. Winch, F. Hayati, D. Boddice, A. Stabrawa, A. Niggebaum, M. Langlois, Y.-H. Lien, S. Lellouch, S. Roshanmanesh, K. Ridley, G. de Villiers, G. Brown, T. Cross, G. Tuckwell, A. Faramarzi, N. Metje, K. Bongs, and M. Holynski, "Quantum sensing for gravity cartography," *Nature* **602**(7898), 590–594 (2022).
36. P. Cheiney, L. Fouché, S. Templier, F. Napolitano, B. Battelier, P. Bouyer, and B. Barrett, "Navigation-Compatible Hybrid Quantum Accelerometer Using a Kalman Filter," *Phys. Rev. Appl.* **10**(3), 034030 (2018).
37. X. Zhang, J. Zhong, B. Tang, X. Chen, L. Zhu, P. Huang, J. Wang, and M. Zhan, "Compact portable laser system for mobile cold atom gravimeters," *Appl. Opt.* **57**(22), 6545–6551 (2018).
38. Y. Bidel, N. Zahzam, C. Blanchard, A. Bonnin, M. Cadoret, A. Bresson, D. Rouxel, and M. F. Lequentrec-Lalancette, "Absolute marine gravimetry with matter-wave interferometry," *Nat. Commun.* **9**(1), 627 (2018).
39. V. Xu, M. Jaffe, C. D. Panda, S. L. Kristensen, L. W. Clark, and H. Müller, "Probing gravity by holding atoms for 20 seconds," *Science* **366**(6466), 745–749 (2019).
40. Y. Bidel, N. Zahzam, A. Bresson, C. Blanchard, M. Cadoret, A. V. Olesen, and R. Forsberg, "Absolute airborne gravimetry with a cold atom sensor," *J. Geod.* **94**(2), 20 (2020).
41. M. Schmidt, M. Prevedelli, A. Giorgini, G. M. Tino, and A. Peters, "A portable laser system for high-precision atom interferometry experiments," *Appl. Phys. B* **102**(1), 11–18 (2011).
42. V. Schkolnik, O. Hellmig, A. Wenzlawski, J. Grosse, A. Kohfeldt, K. Döringshoff, A. Wicht, P. Windpassinger, K. Sengstock, C. Braxmaier, M. Krutzik, and A. Peters, "A compact and robust diode laser system for atom interferometry on a sounding rocket," *Appl. Phys. B* **122**(8), 217 (2016).
43. Q. Wang, Z. Wang, Z. Fu, W. Liu, and Q. Lin, "A compact laser system for the cold atom gravimeter," *Opt. Commun.* **358**, 82–87 (2016).
44. S. Kulas, C. Vogt, A. Resch, J. Hartwig, S. Ganske, J. Matthias, D. Schlippert, T. Wendrich, W. Ertmer, E. Maria Rasel, M. Damjanic, P. Weßels, A. Kohfeldt, E. Luvsandamdin, M. Schiemangk, C. Grzeschik, M. Krutzik, A. Wicht, A. Peters, S. Herrmann, and C. Lämmerzahl, "Miniaturized Lab System for Future Cold Atom Experiments in Microgravity," *Microgravity Sci. Technol.* **29**(1-2), 37–48 (2017).
45. Q. Luo, H. Zhang, K. Zhang, X.-C. Duan, Z.-K. Hu, L.-L. Chen, and M.-K. Zhou, "A compact laser system for a portable atom interferometry gravimeter," *Rev. Sci. Instrum.* **90**(4), 043104 (2019).
46. C. D. Macrae, K. Bongs, and M. Holynski, "Optical frequency generation using fiber bragg grating filters for applications in portable quantum sensing," *Opt. Lett.* **46**(6), 1257–1260 (2021).
47. D. O. Sabulsky, J. Junca, G. Lefèvre, X. Zou, A. Bertoldi, B. Battelier, M. Prevedelli, G. Stern, J. Santoire, Q. Beauvils, R. Geiger, A. Landragin, B. Desruelle, P. Bouyer, and B. Canuel, "A fibered laser system for the MIGA large scale atom interferometer," *Sci. Rep.* **10**(1), 3268 (2020).
48. S. Sarkar, R. Piccon, S. Merlet, and F. P. dos Santos, "Simple and robust architecture of a laser system for atom interferometry," *Opt. Express* **30**(3), 3358–3366 (2022).
49. V. M. Valenzuela, S. Hamzeloui, M. Gutiérrez, and E. Gomez, "Multiple isotope magneto-optical trap from a single diode laser," *J. Opt. Soc. Am. B* **30**(5), 1205–1210 (2013).
50. X. Wu, F. Zi, J. Dudley, R. Bilotta, P. Canoza, and H. Müller, "Multiaxis atom interferometry with a single-diode laser and a pyramidal magneto-optical trap," *Optica* **4**(12), 1545–1551 (2017).
51. J. Fang, J. Hu, X. Chen, H. Zhu, L. Zhou, J. Zhong, J. Wang, and M. Zhan, "Realization of a compact one-seed laser system for atom interferometer-based gravimeters," *Opt. Express* **26**(2), 1586–1596 (2018).
52. B. Wu, Y. Zhao, B. Cheng, C. Zhang, D. Li, D. Zhu, Y. Yue, J. Li, K. Zhang, Q. Lin, and K. Weng, "A Simplified Laser System for Atom Interferometry Based on a Free-Space EOM," *Photonics* **9**(5), 301 (2022).
53. D. Huang, M. A. Tran, J. Guo, J. Peters, T. Komljenovic, A. Malik, P. A. Morton, and J. E. Bowers, "High-power sub-kHz linewidth lasers fully integrated on silicon," *Optica* **6**(6), 745–752 (2019).
54. S. Chiow and N. Yu, "Compact atom interferometer using single laser," *Appl. Phys. B* **124**(6), 96 (2018).
55. C. Rammeloo, L. Zhu, Y.-H. Lien, K. Bongs, and M. Holynski, "Performance of an optical single-sideband laser system for atom interferometry," *J. Opt. Soc. Am. B* **37**(5), 1485 (2020).
56. L. Zhu, Y.-H. Lien, A. Hinton, A. Niggebaum, C. Rammeloo, K. Bongs, and M. Holynski, "Application of optical single-sideband laser in Raman atom interferometry," *Opt. Express* **26**(6), 6542–6553 (2018).
57. M. A. Maldonado, W. M. Pimenta, J. A. Franco-Villafañe, and E. Gomez, "Elimination of spatial Rabi frequency modulation by sideband suppression with a calcite crystal," *Appl. Phys. B* **127**(12), 170 (2021).
58. Q. Luo, H. Zhou, L. Chen, X. Duan, M. Zhou, and Z. Hu, "Eliminating the phase shifts arising from additional sidebands in an atom gravimeter with a phase-modulated Raman laser," *Opt. Lett.* **47**(1), 114 (2022).
59. N. Arias, V. Abediyeh, S. Hamzeloui, and E. Gomez, "Low phase noise beams for Raman transitions with a phase modulator and a highly birefringent crystal," *Opt. Express* **25**(5), 5290–5301 (2017).
60. R. Karcher, F. P. Dos Santos, and S. Merlet, "Impact of direct-digital-synthesizer finite resolution on atom gravimeters," *Phys. Rev. A* **101**(4), 043622 (2020).
61. O. Carraz, R. Charrière, M. Cadoret, N. Zahzam, Y. Bidel, and A. Bresson, "Phase shift in an atom interferometer induced by the additional laser lines of a Raman laser generated by modulation," *Phys. Rev. A* **86**(3), 033605 (2012).

62. S. M. Dickerson, J. M. Hogan, A. Sugarbaker, D. M. S. Johnson, and M. A. Kasevich, "Multiaxis Inertial Sensing with Long-Time Point Source Atom Interferometry," *Phys. Rev. Lett.* **111**(8), 083001 (2013).
63. S. Martínez, L. Hernández, D. Reyes, E. Gomez, M. Ivory, C. Davison, and S. Aubin, "Note: Fast, small, and low vibration mechanical laser shutters," *Rev. Sci. Instrum.* **82**(4), 046102 (2011).
64. S. Hamzeloui, D. Martínez, V. Abediyeh, N. Arias, E. Gomez, and V. M. Valenzuela, "Dual atomic interferometer with a tunable point of minimum magnetic sensitivity," *Phys. Rev. A* **94**(3), 033634 (2016).
65. J. M. Cervantes, M. A. Maldonado, J. A. F-V. ne, T. Roach, V. M. Valenzuela, and E. Gomez, "Selection of a Raman beam waist in atomic gravimetry," *OSA Continuum* **4**(7), 1996–2007 (2021).
66. G. A. Olivares-Rentería, D. A. Lancheros-Naranjo, E. Gomez, and J. A. Franco-Villafa ne, "Quantum gravimetry in the same internal state using composite light Raman pulses," *Phys. Rev. A* **101**(4), 043613 (2020).
67. A. Louchet-Chauvet, T. Farah, Q. Bodart, A. Clairon, A. Landragin, S. Merlet, and F. Pereira Dos Santos, "The influence of transverse motion within an atomic gravimeter," *New J. Phys.* **13**(6), 065025 (2011).